Chemical Science

ROYAL SOCIETY OF CHEMISTRY

EDGE ARTICLE

View Article Online
View Journal | View Issue



Cite this: *Chem. Sci.*, 2026, **17**, 1822

All publication charges for this article have been paid for by the Royal Society of Chemistry

# Regulating the photoelectric properties of porphyrin-based COF nanozymes by pillararene with polyphenol structure for efficient photo-enhanced antibacterial effect

Yahui Liu,†[a] Jia Wen, †*[b] Bingqian Ge,[a] Tingting Guo,[a] Jiaqi Li,[a] Lingshan Jia,[a] Shoupeng Cao,[c] Wei Li *[a] and Kui Yang *[a]

Nanozymes show great potential as alternatives to natural enzymes. Covalent organic frameworks (COFs) have attracted huge attention for the design of nanozymes due to their unique structures and intriguing properties. Incorporation of appropriate building blocks into COFs can endow them with specific properties, allowing the possibility to design highly efficient COF-based nanozymes. Herein, a heteroporous COF (COF-P5–OH–Fe) was designed and constructed by introducing pillar[5]arenes with polyphenol structures into the porphyrin-based COFs through post-modification strategies, and subsequently, Fe was further modified on the COFs through coordination. The obtained COF-P5–OH–Fe nanozyme showed outstanding peroxidase-like activity, the catalytic activity of which could be enhanced efficiently under light irradiation. The unique polyphenol motif of pillar[5]arenes endows COF-P5–OH–Fe with a narrow energy band gap and enhanced photocurrent and improves the circulation of $Fe^{3+}/Fe^{2+}$. As a result, the activity of COF-P5–OH–Fe nanozyme was enhanced to generate reactive oxygen species, enabling efficient antibacterial action. In particular, the absorption wavelength of the COF-P5–OH–Fe nanozyme, which was around 986 nm, enabled it to exhibit superior photo-enhanced bactericidal activity under near-infrared light irradiation. Furthermore, the antibacterial mechanism was also investigated by genome-wide transcriptome analysis using RNA sequencing.

Received 22nd August 2025
Accepted 11th November 2025

DOI: 10.1039/d5sc06433c

rsc.li/chemical-science



## Introduction

Natural enzymes are catalysts for thousands of biological reactions that exist in nature. However, due to their high isolation and purification cost and difficult storage, researchers have been forced to start exploring alternatives. Nanozymes are an emerging type of nanomaterials with enzyme-like properties, including peroxidase (POD), oxidase (OXD), *etc.*[1–4] They have been developed to simulate various natural enzymes due to their advantages, such as low cost, high stability and suitability for large-scale production. Among various reported nanozymes, POD-like nanozymes have attracted extensive attention. The properties of POD-like nanozymes are similar to those of natural PODs, which catalyze the oxidation of substrates. For POD-like nanozymes, the cycling of $Fe^{3+}/Fe^{2+}$ is one of the key factors affecting the catalytic activity.[5] For example, Meng's group designed and synthesized a bimetallic FeNi-MOF nanozyme.[6] The potential difference between Fe and Ni can accelerate the rate of the $Fe^{3+}/Fe^{2}$ cycle, efficiently enhancing the catalytic activity of the nanozyme. To further establish nanozymes a better alternative to natural enzymes, scientists are constantly exploring effective strategies to enhance their catalytic activity, such as controlling their size, shape and composition, surface modification, defect engineering, and applying external stimuli.[1,7–11] Among these strategies, the use of light irradiation to enhance the catalytic activity holds great application potential, mainly because it enables effective control, spatiotemporal accuracy and environmental friendliness.[12,13] Therefore, accelerating the $Fe^{3+}/Fe^{2+}$ cycle and introducing photo-responsive motifs are expected to yield highly active POD-like nanozymes.

Covalent organic frameworks (COFs), with their permanent porosity and highly ordered structures, have emerged as a significant material class for the construction of nanozymes due to their customizable optoelectronic properties and active site architectures.[14–16] With the pre-designable nature of COFs, their light-harvesting and charge-transport properties can be triggered by introducing a functional group into the periodic backbones and built-in pores. Numerous efforts have focused on the

[a]*State Key Laboratory of New Pharmaceutical Preparations and Excipients, Key Laboratory of Medicinal Chemistry and Molecular Diagnosis of the Ministry of Education, College of Chemistry and Materials Science, Hebei University, Baoding 071002, P. R. China. E-mail: liweihebeilab@163.com; yangkuihbu@126.com*

[b]*College of Pharmaceutical Science, Hebei University, Baoding 071002, P. R. China. E-mail: wenjiahbu@163.com*

[c]*State Key Laboratory of Polymer Materials Engineering, College of Polymer Science and Engineering, Sichuan University, Chengdu 610065, P. R. China*

† These authors contributed equally to this work.

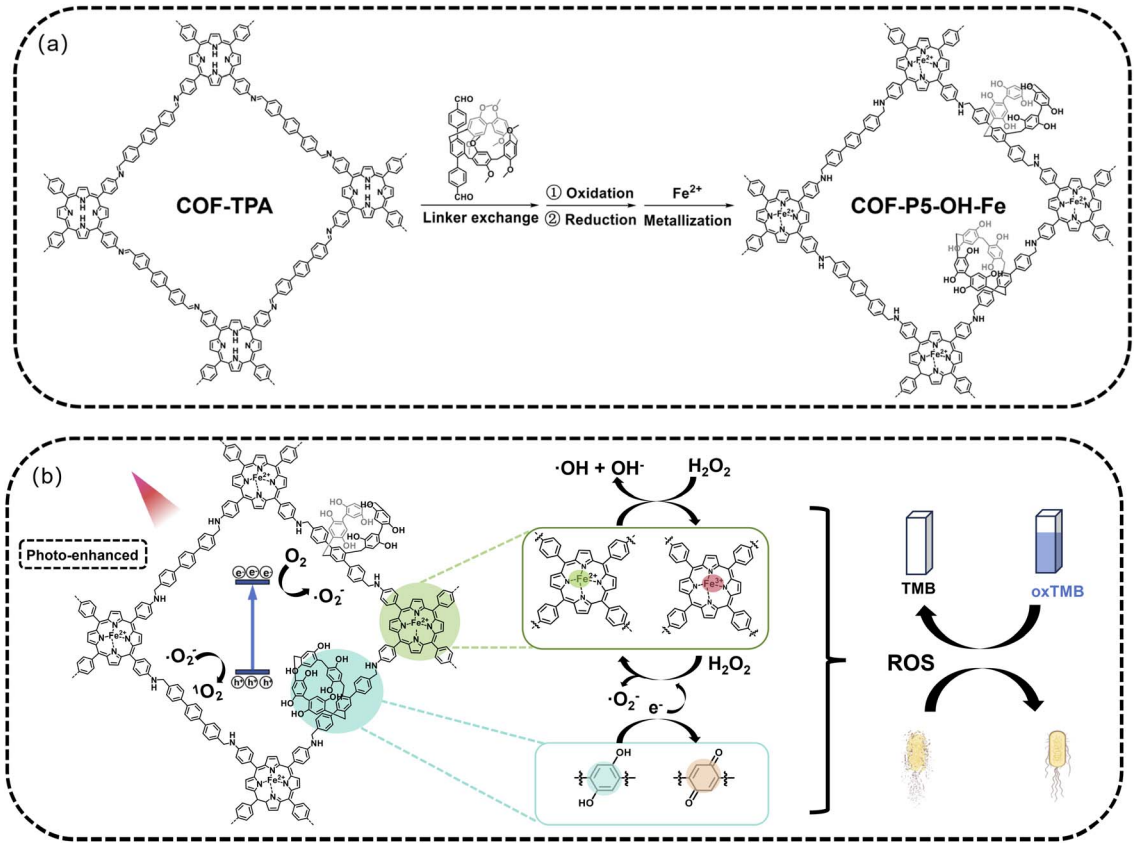


Scheme 1 Preparation and applications of COF-P5–OH–Fe.

incorporation of functional groups into COFs to enhance their photocatalytic performance. For example, some previous studies introduced porphyrin, which has unique photophysical properties, into COFs to design photo-active nanozymes.[17,18] In addition, the incorporation of electron-rich units into COFs has been demonstrated to be an effective strategy to facilitate high charge transfer mobility and regulate the band gap and energy levels to increase visible light adsorption.[19,20] Therefore, the molecular-level rational design of COFs with electron-rich units opens pathways for optimizing these properties to boost photocatalytic performance.

Pillar[n]arenes, a class of macrocyclic hosts, have electron-rich cavities and rigid ring structures.[21] They are expected to provide an innovative approach to enrich the applications of COFs or covalent organic polymers.[22–25] Herein, a photo-enhanced nanozyme with macrocyclic structure (COF-P5–OH–Fe) was synthesized and constructed by introducing pillar[5]arenes with polyphenol structures into the porphyrin-based COFs through post-modification strategies, then further modified with Fe through coordination (Scheme 1). To demonstrate the critical role of pillar[5]arenes with polyphenol structures—which could store electrons and protons, accelerate the $Fe^{3+}$/$Fe^{2+}$ recycle and promote the Fenton or Fenton-like reactions[26,27]—COFs without pillar[5]arene moieties, without polyphenol structures, and without Fe modification were also prepared as control groups. The results demonstrated that the unique polyphenol structure endowed COF-P5–OH–Fe with a narrow energy band gap and efficient electron transfer, promoting the reduction of $Fe^{3+}$ and effectively enhancing its photoactivated POD-like bactericidal activity.

## Results and discussion

### Characterizations of COFs

To obtain COFs derived from pillar[5]arene, the functionalized pillar[5]arene (CHO–P5) was synthesized according to a reported procedure (Scheme S1),[22] then characterized using $^1$H NMR (Fig. S1–S4). Subsequently, the parent COF-TPA was synthesized through a Schiff-base condensation reaction of 4,4″-*p*-terphenyldicarboxaldehyde (TPA) with 5,10,15,20-tetrakis(4-aminophenyl)porphyrin (TAPP) by the solvothermal method. Then, COF-P5 was synthesized using COF-TPA as a core and CHO–P5 as a new linker using a partial linker exchange strategy.[22,28,29] Further, COFs derived from pillar[5]arene with polyphenol structures (COF-P5–OH) were obtained through an oxidation–reduction process. Finally, $Fe^{2+}$ was introduced into the COFs by coordination.[30] The comprehensive synthetic routes for these compounds are depicted in Schemes S2–S5. To demonstrate the successful COF-to-COF transformation, a series of chemical and microstructural characterizations of COF-TPA, COF-P5, COF-P5=O, COF-P5–OH and COF-P5–OH–Fe were conducted. The crystalline structures of all COFs were determined using powder X-ray diffraction (PXRD).

Fig. 1a indicates that COF-TPA has a strong diffraction peak at $2\theta = 2.46°$ and a weak diffraction peak at approximately $2\theta =$

5.1°, which belong to the (100) crystal plane and the (200) crystal plane, respectively, indicating that COF-TPA has a relatively high crystallinity. The cell parameters of COF-TPA were estimated to be $a = 35.01$ Å, $b = 35.01$ Å, $c = 3.63$ Å, and $\alpha = \beta = \gamma = 90°$, as evidenced by the small agreement factors of $R_p = 6.03\%$ and $R_{wp} = 8.76\%$, demonstrating good agreement. The PXRD patterns of COF-TPA and the series of COFs (derived from pillar[5]arene) were similar, although the latter showed a gradually decreasing peak intensity (Fig. 1b and S5). It was speculated that during the oxidation–reduction of COF-P5, some of the imine bonds in the COF skeleton were cleaved, reducing the crystallinity of the material. The FT-IR spectra of both COF-TPA and COF-P5 showed the disappearance of the aldehyde peak at 1678 $cm^{-1}$ and amine peaks at 3435 and 3332 $cm^{-1}$.[31,32] Meanwhile, the appearance of the C=N characteristic peak at 1627 $cm^{-1}$ supported the formation of imine bonds *via* the condensation of aldehyde and primary amine (Fig. S6a and 1c).[31,32] Besides, to confirm the presence of both the original TPA and exchanged CHO–P5 linkers in COF-P5, hydrolysis experiment was performed. Concentrated HCl was used to hydrolyze the COF–P5 powder, which was subsequently analyzed by $^1$H NMR spectroscopy. The resulting spectrum revealed simultaneous proton peaks corresponding to TPA (10.05 ppm) and CHO–P5 (10.00 ppm) aldehyde groups (Fig. S7), indicating the successful occurrence of the linker exchange reaction. Multiple peaks can be seen in the range 7.73–6.50 ppm, which are the characteristic peaks of CHO–P5. The results indicated that CHO–P5 successfully replaced some of the TPA units in COF-TPA. By integrating the peak area of the aldehyde group region, it was determined that the degree of linker exchange of CHO–P5 was approximately 16.7%.

In addition, the FT-IR results in Fig. 1c also demonstrated the successful preparation of COF-P5=O, COF-P5–OH and COF-P5–OH–Fe. Specifically, a characteristic stretching vibration peak of the methoxy group (C–O–C) of pillar[5]arene appeared at 1211 $cm^{-1}$ in the spectrum of COF-P5 (black line).[22] After oxidation treatment, the C–O–C peak and the imine (C=N) characteristic peak were significantly weakened. Meanwhile, a new carbonyl absorption peak (C=O) appeared at 1697 $cm^{-1}$, indicating that the methoxy group of the pillar[5]arene was oxidized and removed to form a quinone structure.[27] Comparison of COF-P5=O and COF-P5–OH revealed that the peak intensity of C=O was reduced, and a new absorption peak emerged in the hydroxyl

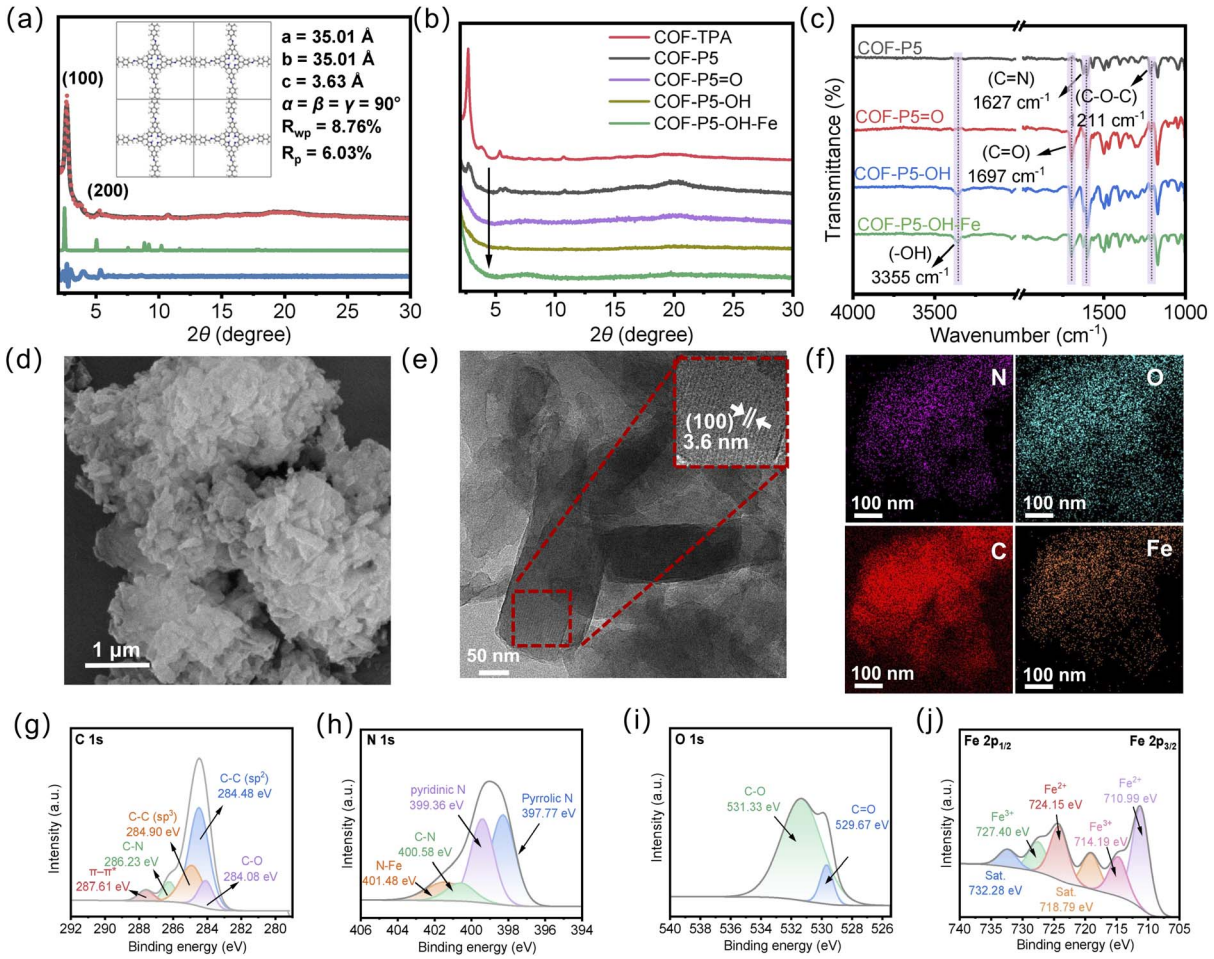


Fig. 1 (a) PXRD pattern of COF-TPA (red: experimental data, black: refined pattern, green: simulation for AA eclipsed, blue: difference); (b) PXRD patterns of COF-TPA, COF-P5, COF-P5=O, COF-P5–OH and COF-P5–OH–Fe; (c) FT-IR spectra of COF-P5, COF-P5=O, COF-P5–OH and COF-P5–OH–Fe; (d) SEM image of COF-P5–OH–Fe; (e) HRTEM image of COF-P5–OH–Fe; (f) elemental mapping of COF-P5–OH–Fe; XPS spectra of COF-P5–OH–Fe: (g) C 1s; (h) N 1s; (i) O 1s; (j) Fe 2p.

characteristic region, confirming that the carbonyl groups in quinone were reduced to phenolic hydroxyl groups. The above results confirmed the successful conversion of COF-P5 to COF-P5–OH through the oxidation–reduction two-step reaction. This COF-P5–OH was further coordinated with $Fe^{2+}$ to obtain the final material COF-P5–OH–Fe.

The detailed morphologies were monitored by scanning electron microscopy (SEM) and transmission electron microscopy (TEM). As shown in Fig. S6b–d, COF-TPA exhibited nanosheet-like crystals with uniform morphology, and the HRTEM image revealed obvious lattice fringes (3.5 nm), which corresponded well to the (100) crystal face. After COF-to-COF transformation, the morphologies of COF-P5, COF-P5=O, COF-P5–OH and COF-P5–OH–Fe changed a little, but still maintained the nanosheet morphology (Fig. 1d, e, S8 and S9). In addition, the TEM-mapping results indicated that COF-P5–OH–Fe contained the uniformly distributed N, C, O and Fe (Fig. 1f). The surface chemical state and elemental composition of the series of COFs were analyzed using X-ray photoelectron spectroscopy (XPS). Fig. S10a, b, e, i and m show the full spectra of COF-P5–OH–Fe, COF-TPA, COF-P5, COF-P5=O and COF-P5–OH, respectively. Through comparative analysis, it can be obtained that these COFs all have three elements: C, N, and O. Moreover, the relative content of O in COF-P5 was higher than that in COF-TPA, which was attributed to the content of O in pillar[5]arenes, indicating the successful introduction of pillar[5]arenes. The C 1s fine spectra indicated that both COF-TPA and COF-P5 retained the peak of the C=N bond at around 286 eV (Fig. S10c and f).[33] Moreover, a C–O–C peak appeared at around 284 eV in COF-P5, corresponding to the methoxy group in the pillar[5]arenes (Fig. S10f). As for the fine spectra of N 1s, COF-P5–OH–Fe has an additional N–Fe peak at about 401 eV, which was produced by the coordination of Fe with the porphyrin cavity (Fig. 1h).[34,35] As for the fine spectra of O 1s (Fig. S10h, l, p and 1i), the spectrum of COF-P5–OH can be fitted to two components: C–O (benzoquinone/phenoxy) and C=O (the broken imine), further confirming that COF-TPA was transformed into COF-P5–OH through oxidation–reduction process, and the partial cleavage of the imine bond. The valence state distribution of Fe in COF-P5–OH–Fe was further analyzed. The Fe 2p spectrum showed that the peaks at 710.99 eV and 724.15 eV corresponded to the $2p_{3/2}$ and $2p_{1/2}$ orbitals of $Fe^{2+}$, respectively, while the peaks at 714.19 eV and 727.40 eV belonged to the $2p_{3/2}$ and $2p_{1/2}$ orbitals of $Fe^{3+}$ (Fig. 1j).[36] This indicated that the coordinated $Fe^{2+}$ was partially oxidized to $Fe^{3+}$.

To explore the thermal stability of the series of COFs, thermogravimetric analysis (TGA) was conducted. The results showed that all COFs maintained good thermal stability below 400 °C (Fig. S11). Furthermore, the remaining content of COF-P5–OH–Fe after high-temperature heating was higher than that of COF-P5–OH. It was speculated that this was caused by the metal oxides produced by Fe, indicating the successful introduction of $Fe^{2+}$. In addition, the content of $Fe^{2+}$ quantitatively analyzed by inductively coupled plasma spectroscopy (ICP) was about 2.4%.

### Photoelectrochemical properties of COFs

The optical properties of the as-prepared COFs derived from pillar[5]arene were first investigated by UV-vis diffuse reflectance spectroscopy (UV-vis DRS). As shown in Fig. S12 and 2a, the edge-banded absorption wavelengths of COF-TPA, COF-P5, COF-P5=O, COF-P5–OH, COF-P5–OH–Fe, COF-TPA–Fe and COF-P5–Fe were 735, 722, 770, 764, 986, 928 and 972 nm, respectively. COF-P5–OH–Fe showed excellent edge-banded absorption, which was caused by the structure of pillar[5]arene and $Fe^{2+}$ synergistically. Based on the Kubelka–Munk function, the corresponding COF-P5–OH–Fe showed the band gap of 1.39 eV in Fig. 2b (the band gaps of other COFs are shown in Fig. S12). To further investigate the energy-level alignment of the COFs, Mott–Schottky curves were measured, and the positive slope is shown in Fig. 2c and S13, which revealed the n-type characteristic of the series of COFs. The $E_{VB}$ of the vacuum energy level of the series of COFs was calculated according to the formula ($E_{VB,NHE} = \varphi + E_{VB\ XPS} - 4.44$) based on the valence band $E_{VB}$ evaluated by VB-XPS (Fig. 2d and S14).[31] The specific band positions of the prepared COFs are illustrated in Fig. 2e. COF-P5–OH–Fe had the smallest $E_g$, indicating that the material can stimulate electron transitions within the material by absorbing photons of lower energy. In addition, the $E_{CB}$ energy level of COF-P5–OH–Fe was lower than the $O_2/{}^{\bullet}O_2^-$ redox potential (−0.33 eV *vs.* NHE), which indicated that under thermodynamically allowable conditions, $O_2$ can be reduced to ${}^{\bullet}O_2^-$. Compared with COF-TPA–Fe and COF-P5–Fe, COF-P5–OH–Fe exhibited a more negative $E_{CB}$, indicating a stronger proton reduction driving force.

The exceptional photoelectronic properties of COF-P5–OH–Fe prompted us to further investigate its electronic properties with electrochemical impedance spectroscopy (EIS), photocurrent responses and photoluminescence (PL) emission spectroscopy. As shown in Fig. 2f, the introduction of pillar[5]arene can reduce the charge transfer resistance of COF, and after conversion to the polyphenol structure, the charge transfer resistance was even smaller. After the introduction of $Fe^{2+}$, the charge transfer resistance was further reduced. It was indicated that COF-P5–OH–Fe effectively reduced the charge transfer resistance.

The transient photocurrent responses of the as-prepared COFs with several on–off cycles of intermittent visible light irradiation were studied. As shown in Fig. 2g and h, under the irradiation of visible light, COF-P5–OH–Fe exhibited an obvious enhanced photocurrent compared with COF-TPA, indicating that the photogenerated charge in COF-P5–OH–Fe could be separated. Whereas, the photocurrent densities of COF-P5–OH and COF-TPA–Fe were not enhanced, indicating that only the polyphenol-structured pillar[5]arenes with Fe can synergically accelerate the photo-response of COF and thereby enhance the separation and transfer of photogenerated charge carriers. The recombination efficiency of photogenerated electrons in COFs was evaluated through PL emission spectroscopy. PL emission spectra originating from the recombination of free charge carriers were applied to disclose the photoinduced interfacial charge dynamics of semiconductors. The lower PL intensity corresponds to the higher separation efficiency of photogenerated electron–hole pairs. As shown in Fig. 2i, the intensity of the PL peak of COF-P5–OH–Fe was weaker than those of other COFs, demonstrating that the introduction of pillar[5]arenes with polyphenol structure and the coordination effect of Fe had

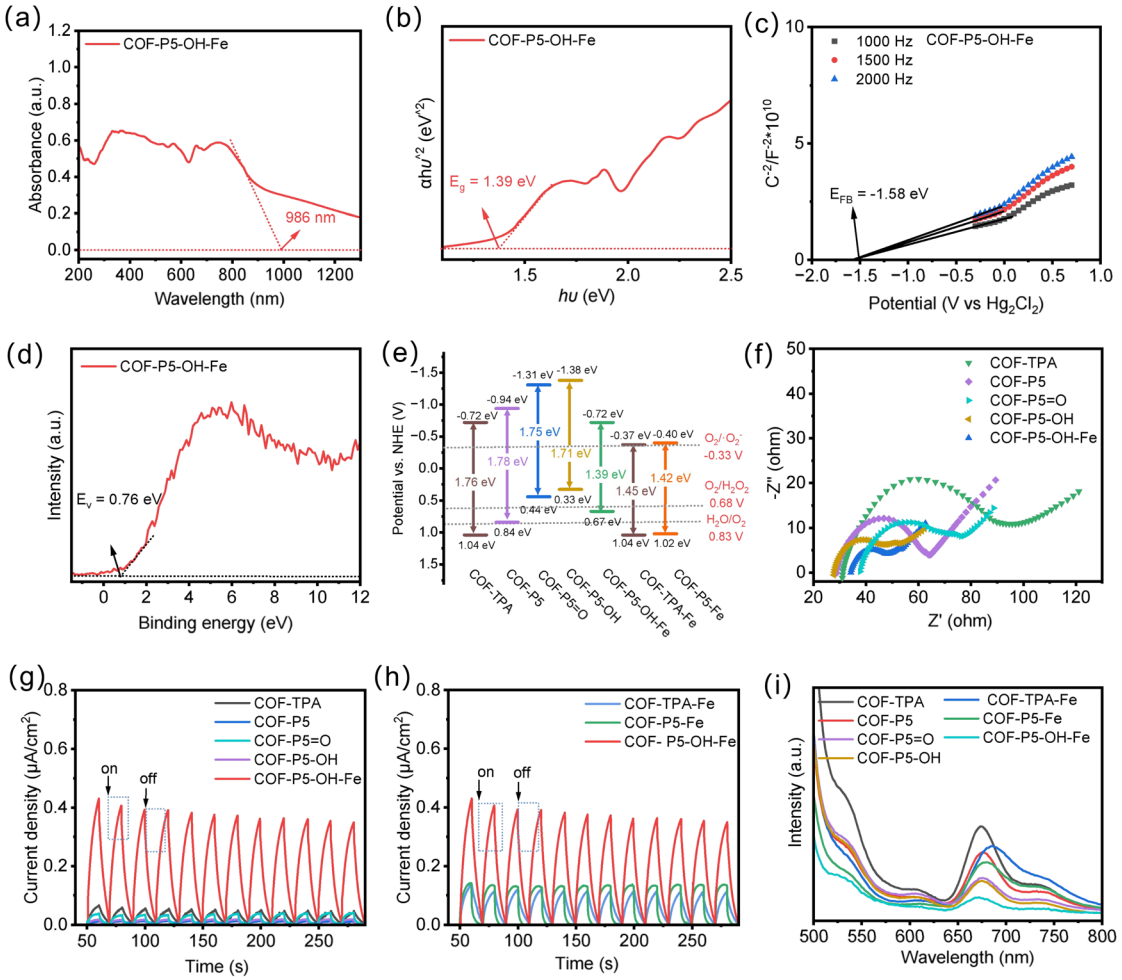


Fig. 2 (a) UV-vis DRS spectrum of COF-P5–OH–Fe; (b) Tauc band gap plots of COF-P5–OH–Fe; (c) Mott–Schottky plots of COF-P5–OH–Fe; (d) VB-XPS plots of COF-P5–OH–Fe; (e) electronic band structure diagrams of various samples; (f) Nyquist plots of EIS spectra of various samples; (g and h) the transient optical responses of various samples and (i) PL spectra of various samples.

the ability to inhibit the electron–hole pair recombination, thereby enhancing the photocatalytic activity.

### Photocatalytic activity of COFs

To demonstrate the catalytic activities of COFs as mimetic PODs, the catalytic oxidation of 3,3,5,5-tetramethylbenzidine (TMB) in the presence of $H_2O_2$ was determined. As illustrated in Fig. 3a and b, compared with other COFs, COF-P5–OH–Fe exhibited the strongest POD-like activity, which was approximately 2.5 times that of COF-P5–Fe. In particular, COF-P5–OH–Fe also exhibited a relatively high POD-like activity in the dark, but slightly lower than that under light conditions. It was indicated that COF-P5–OH–Fe can enhance the POD-like activity of COFs by promoting the Fenton-like reaction. Further, the photo-controllable catalytic performance of COF-P5–OH–Fe was studied by alternating treatment of white light irradiation and darkness. As shown in Fig. 3c, under dark conditions, the absorption value at 652 nm increased, indicating that COF-P5–OH–Fe exhibited POD-like activity, which was ascribed to Fenton reaction. By comparing the adjacent slopes for light irradiation and non-light irradiation, it can be observed that the slope was slightly larger under light exposure, indicating that light irradiation can accelerate the catalytic reaction. To further demonstrate the catalytic activities of COFs as mimetic OXDs, TMB was employed as chromogenic substrate to evaluate the photocatalytic properties of the as-prepared COFs. As shown in Fig. S15, the as-prepared series of COFs could all oxidize TMB slightly, showing a certain level of photo-oxidase activity, but the difference among COF-P5–OH, COF-P5–Fe, COF-TPA–Fe and COF-P5–OH–Fe was not significant. This indicated that the post-functionalization of COFs using pillar[5]arenes and polyphenol structures, as well as the coordination of $Fe^{2+}$, did not essentially enhance the oxidase activity of COFs. To determine the optimal pH conditions for COF-P5–OH–Fe catalysis, the test conditions were maintained constant, with only the pH value varied. The optimal POD-like activity conditions were determined by comparing $A_{652\ nm}$. The results indicated that the optimal pH conditions for the POD-like activity of COF-P5–OH–Fe in both darkness and light were 4.0 (Fig. 3d). Further, the POD-like activity of COF-P5–OH–Fe was detected based on the steady-state kinetics by altering the concentration of TMB or $H_2O_2$ to obtain $K_m$ and $V_{max}$. As shown in Fig. 3e, f,

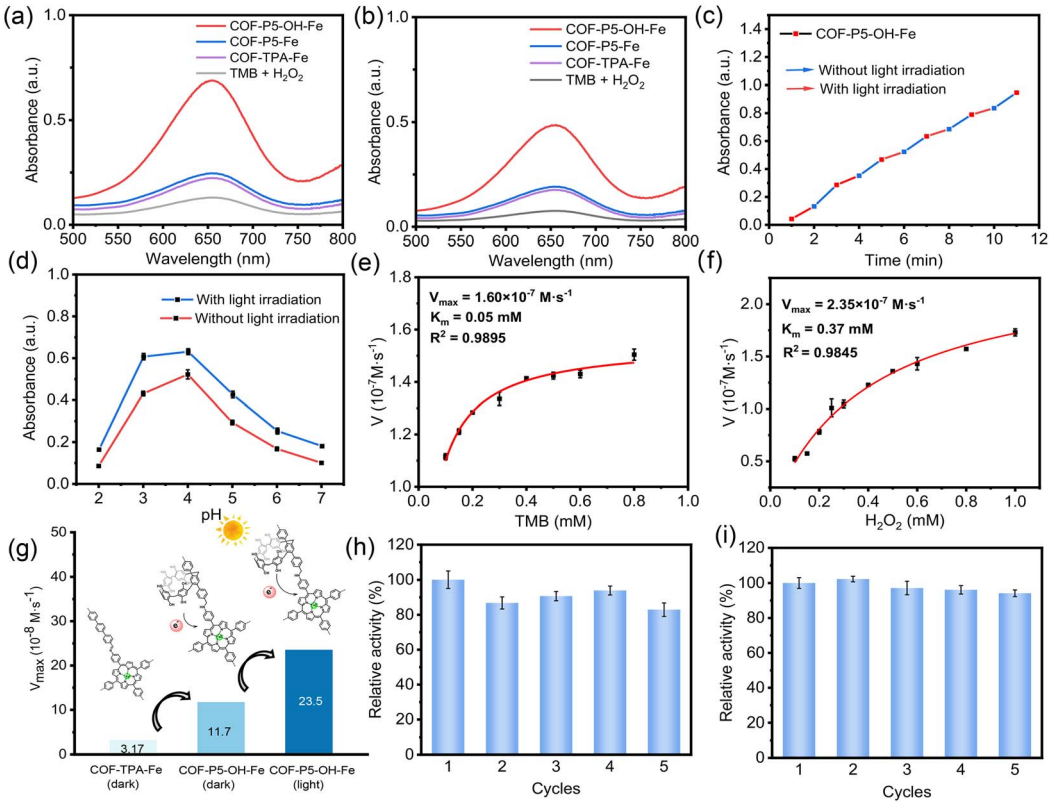


Fig. 3 POD-like activity of different samples (a) under white light irradiation and (b) in the dark condition. (c) Photo-controllable POD-like activity of COF-P5–OH–Fe. (d) Relative POD-like activity of COF-P5–OH–Fe at different pH values with and without light irradiation. Steady-state kinetic Lineweaver–Burk plots of COF-P5–OH–Fe under the irradiation of white light with (e) varying TMB concentrations or (f) varying $H_2O_2$ concentrations. (g) The comparison of $V_{max}$ of COF-TPA–Fe (dark), COF-P5–OH–Fe (dark) and COF-P5–OH–Fe (light) with varying $H_2O_2$ concentrations. Relative changes in POD-like activity of COF-P5–OH–Fe over 1–5 cycles (h) with white light irradiation and (i) without light irradiation.

S16, S17 and S18, the $V_{max}$ of COF-P5–OH–Fe with white light irradiation was over 7 times that of COF-P5–OH–Fe and over twice that of COF-TPA–Fe without light irradiation. When compared with most of the reported nanozymes (Table S1), COF-P5–OH–Fe also had a smaller $K_m$ and a larger $V_{max}$, indicating that COF-P5–OH–Fe showed good affinity and highly efficient catalytic performance. Notably, the POD-like activity was well maintained after five cycles (Fig. 3h and i). In addition, the results of FT-IR, TEM and XPS indicated that the structure and morphology of COF-P5–OH–Fe remained consistent with their primary states after catalysis (Fig. S19).

### Catalytic mechanism of COFs

To deeply analyze the influence of pillar[5]arenes with polyphenol structure on the catalytic activity of COFs, CV tests were conducted. As displayed in Fig. 4a and S20, in comparison with COF-TPA, COF-P5, COF-P5–OH, and COF-TPA–Fe, COF-P5–OH–Fe had a larger oxidation–reduction current, indicating the enhancing effect of polyphenol structure on the catalytic activity of COFs. In addition, the physical mixture of CHO–P5–OH and COF-TPA–Fe did not show a significant increase in POD-like activity (Fig. 4b and S21), further indicating that the polyphenol-structured pillar[5]arenes (CHO–P5–OH) needed to be embedded in the COF skeleton through covalent bonding rather than a simple physical mixture. Only through this way, the catalytically active sites of the material can be effectively regulated, and its enzyme-like performance can be enhanced. To investigate the POD-like catalytic mechanism of COF-P5–OH–Fe, different types of free radicals were analyzed by comparing the absorption values at 652 nm after adding different free radical scavengers. The variables were as follows: no scavenger (blank), absence of oxygen (under $N_2$), *tert*-butanol (*t*-BuOH, the scavenger of $^{\bullet}OH$), *p*-benzoquinone (PBQ, the scavenger of $^{\bullet}O_2^-$), histidine (His, the scavenger of $^1O_2$) and catalase (CAT, the scavenger of $H_2O_2$). As shown in Fig. 4c and S22, the absence of oxygen ($N_2$-saturated experiment) caused a significant decrease in ox-TMB, suggesting oxygen dissolved in water played an important role in the process of oxidation. The POD-like activity of COF-P5–OH–Fe was significantly inhibited after the addition of PBQ. This indicated that $^{\bullet}O_2^-$ was the reactive oxygen species (ROS) that played a major role in the photocatalysis of COF-P5–OH–Fe. In addition, the POD-like activity of COF-P5–OH–Fe was also inhibited in the presence of *t*-BuOH and His, demonstrating that $^{\bullet}OH$ and $^1O_2$ were also generated in the catalytic reaction system. To further identify the ROS involved, electron paramagnetic resonance (EPR) spectroscopy was employed, which would probe the generation of ROS using 5,5-dimethyl-1-pyridine *N*-oxide (DMPO) and 2,2,6,6-tetramethylpiperidin (TEMP) as spin traps. As shown in Fig. 4d–f, the $^1O_2$,

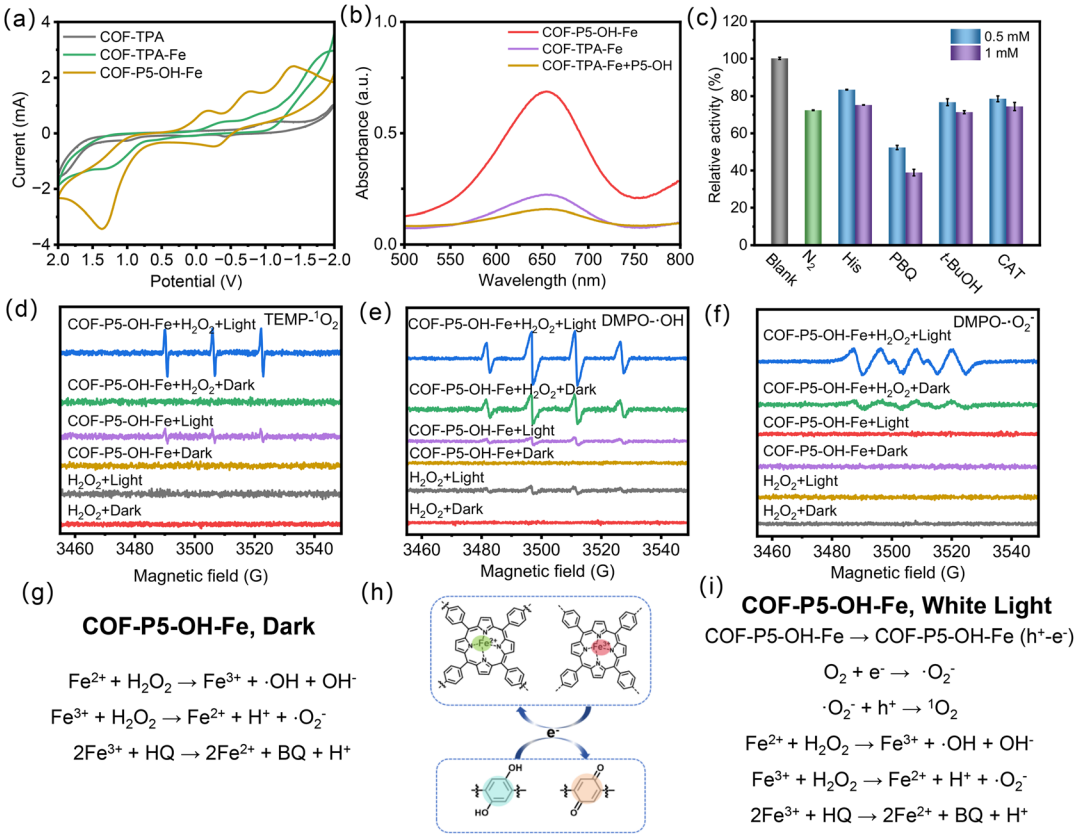


Fig. 4 (a) CV curves of different samples; (b) the POD-like activity of COF-P5–OH–Fe and the physical mixture of COF-TPA–Fe and P5–OH under the irradiation of white light; (c) effects of $N_2$ and different radical scavengers on the POD-like activity of COF-P5–OH–Fe under white light irradiation; EPR spectra of (d) $^1O_2$, (e) $^{\bullet}OH$, (f) $^{\bullet}O_2^-$ under light/dark conditions; (g–i) schematic diagram of the catalytic mechanism of COF-P5–OH–Fe.

$^{\bullet}OH$ and $^{\bullet}O_2^-$ were the main ROS for the photo-responsive catalysis of COF-P5–OH–Fe under white light irradiation. Whereas, under dark conditions, COF-P5–OH–Fe could only generate $^{\bullet}OH$ and $^{\bullet}O_2^-$ in the presence of $H_2O_2$, again verifying the catalytic function of the Fe site. The feasible ROS generation pathways under different conditions are illustrated in Fig. 4g–i. The efficiency of ROS generation by COF-P5–OH–Fe with or without light has been significantly improved through the transfer of electrons based on the benzoquinone structures of pillararene.

## Antibacterial application of COFs

POD has been widely used in antibacterial applications, and the ROS generated by it can destroy bacterial cell membranes and promote cell apoptosis.[37,38] Based on the photo-enhanced POD-like activity of COF-P5–OH–Fe, the antibacterial ability of COF-P5–OH–Fe against *Escherichia coli* (*E. coli*) and *Staphylococcus aureus* (*S. aureus*) was evaluated. As shown in Fig. 5a and b, COF-P5–OH–Fe showed 83% and 94% antibacterial effects on *E. coli* in the presence of $H_2O_2$ under dark and white light irradiation, respectively. COF-P5–OH–Fe also showed good antibacterial effects on *S. aureus* (Fig. S23). It was verified again that COF-P5–OH–Fe generated ROS through POD-like activity, thereby having a strong ability to kill bacteria. In addition, benefiting from the broad absorption wavelength, COF-P5–OH–Fe can also kill 90% of *E. coli* in the presence of $H_2O_2$ under 850 nm light irradiation, demonstrating its potential for the treatment of deeper tissues.

To further investigate the antibacterial mechanism of COF-P5–OH–Fe, *E. coli* treated with nothing (the control group) and COF-P5–OH–Fe with and without white light irradiation were subjected to genome-wide transcriptome analysis using RNA-sequencing (RNA-seq). The principal component and component correlation analyses (PCA) indicated rational concordance of intragroup deviations, confirming the plausibility of the RNA-seq results (Fig. 5c). Compared with the control group, a total of 807 genes showed significant differences in expression for the COF-P5–OH–Fe group under the irradiation of white light ($p < 0.05$, [$\log_2$ foldchange] > 1); specifically, 309 genes were upregulated and 498 genes were downregulated (Fig. S24a). The differentially expressed genes (DEGs) shown in the heatmap presented differences among different groups more intuitively (Fig. S24b). In order to better understand the functions, metabolic pathways, and interactions of DEGs associated with the antibacterial effects, gene ontology (GO) was investigated. As illustrated in Fig. S24c, oxidoreductase activity, transmembrane transporter activity as well as transition metal ion, tetrapyrrole and heme binding were the main terms represented in molecular function ontology. In the ontology of cellular components, the top categories were located in the cell periphery, outer membrane, cell envelope and external encapsulating structure.

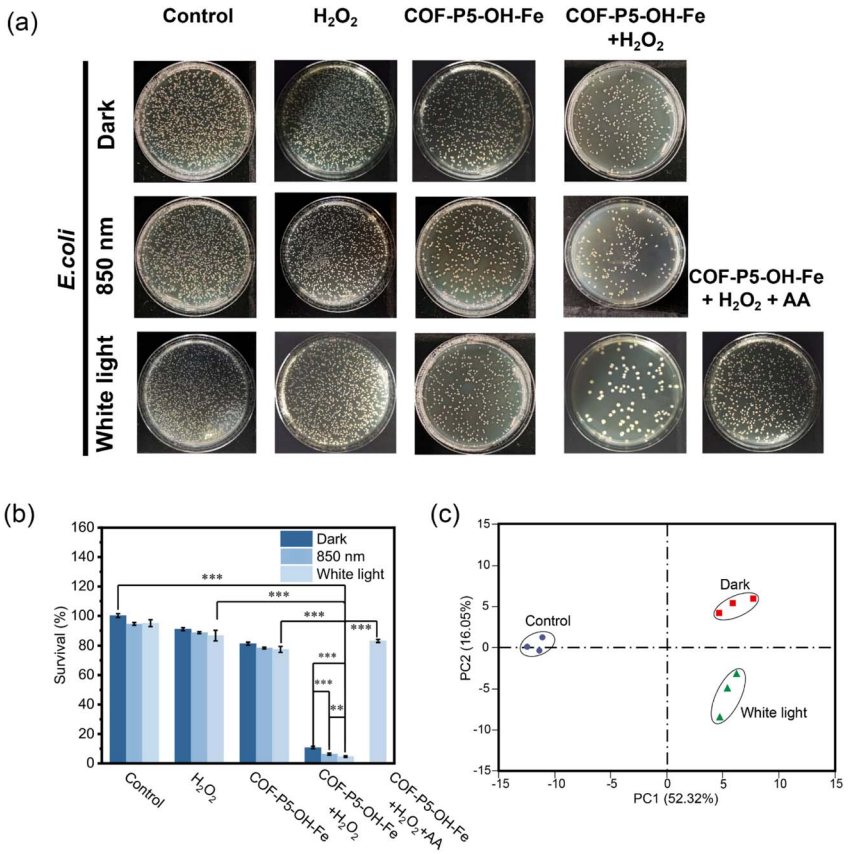


Fig. 5 (a) Photographs of *E. coli* colonies after different treatments. (b) Survival rate of *E. coli* after different treatments. Data are presented as mean ± SD ($n = 3$, ***$p < 0.001$, **$p < 0.01$). Transcriptomic profiling of *E. coli* treated with the control group and COF-P5–OH–Fe samples: (c) PCA of differentially expressed genes determined by whole-transcriptome RNA-seq of *E. coli* in the white light group, dark group and control group.

With regard to the ontology of biological process, the main categories were gathered at carbohydrate transport, electron transport and protein-containing complex assembly. Therefore, the antibacterial mechanism of COF-P5–OH–Fe against Gram-negative bacteria may include interfering with oxidative stress pathways, affecting cell transmembrane transport, and destroying the integrity and structure of the cell wall and membrane. In addition, Kyoto Encyclopedia of Genes and Genome (KEGG) enrichment analysis indicated that the genes which encode key enzymes involved in microbial metabolism, ABC transporters, citrate and nitrogen cycle, oxidative phosphorylation, biosynthesis of arginine, *etc.*, were significantly downregulated (Fig. S24d), suggesting that the metabolism and energy supply were disrupted and that their normal activities were disturbed in the antibacterial processes of COF-P5–OH–Fe. In particular, compared with the group of COF-P5–OH–Fe without light irradiation, some genes related to amino acid biosynthesis and metabolism were further downregulated for the group of COF-P5–OH–Fe with light irradiation (Fig. S24e). The above results demonstrated that under incubation with COF-P5–OH–Fe, bacterial intracellular energy metabolism, oxidative stress and normal expression were seriously disturbed, thereby damaging their membrane integrity and ultimately leading to the death of bacteria.

## Conclusions

In conclusion, a photo-enhanced COF nanozyme, COF-P5–OH–Fe, was successfully constructed through a post-modification strategy based on pillar[5]arenes and porphyrin. Thanks to the synergistic effect of pillar[5]arenes with polyphenol structures and porphyrin–Fe, an obvious reduction in the band gap energy and a distinct enhancement of photocurrent can be achieved to greatly improve the POD-like activity of COF-P5–OH–Fe. Specifically, the pillar[5]arenes with polyphenol structures can provide electrons, reducing $Fe^{3+}$ to $Fe^{2+}$, promoting the Fenton reaction. Eventually, it can efficiently catalyze the generation of ROS, thereby demonstrating superior POD-like activity and effectively inhibiting bacterial growth. In particular, the absorption wavelength of COF-P5–OH–Fe nanozyme enabled it to exhibit superior photo-enhanced bactericidal activity under 850 nm light irradiation. This research provides new insights for the development of efficient nanozymes and their applications in antibacterial therapies.

## Author contributions

K. Yang and J. Wen conceived and designed the research. Y. Liu, B. Ge, T. Guo, J. Li and L. Jia performed the synthesis and

characterization. Y. Liu, B. Ge and T. Guo carried out the photocatalytic activity, catalytic mechanism and application assays. All authors contributed to the discussion and approved the final version of the manuscript.

## Conflicts of interest

There are no conflicts to declare.

## Data availability

Experimental procedures and all relevant data are available in supplementary information (SI) and from the authors. Supplementary information: experimental procedures, the supplementary data of the chemical and microstructural characterizations, photoelectrochemical properties, catalytic activities and antibacterial properties of COFs. See DOI: https://doi.org/10.1039/d5sc06433c.

## Acknowledgements

This work was financially supported by the Natural Science Foundation of Hebei Province (No. B2023201031), Science Research Project of Hebei Education Department (QN2023117), and the Advanced Talents Incubation Program of Hebei University (No. 521000981345 and No. 521000981343).

## Notes and references

1 W. Yang, X. Yang, L. Zhu, H. Chu, X. Li and W. Xu, *Coord. Chem. Rev.*, 2021, **448**, 214170.
2 M. Liang and X. Yan, *Acc. Chem. Res.*, 2019, **52**, 2190–2200.
3 Y. Huang, J. Ren and X. Qu, *Chem. Rev.*, 2019, **119**, 4357–4412.
4 H. Wei and E. Wang, *Chem. Soc. Rev.*, 2013, **42**, 6060–6093.
5 H. Dong, W. Du, J. Dong, R. Che, F. Kong, W. Cheng, M. Ma, N. Gu and Y. Zhang, *Nat. Commun.*, 2022, **13**, 5365.
6 X. Zhao, N. Zhang, T. Yang, D. Liu, X. Jing, D. Wang, Z. Yang, Y. Xie and L. Meng, *ACS Appl. Mater. Interfaces*, 2021, **13**, 36106–36116.
7 M. A. Dheyab, A. A. Aziz, W. Abdullah, S. T. Alanezi, W. H. Kasasbeh, F. Fohely, P. M. Khaniabadi, M. S. Jameel, N. Oladzadabbasabadi and M. Ghasemlou, *ACS Appl. Bio Mater.*, 2025, **8**, 4514–4548.
8 Y. Ji, Y. Wang, H. Wang, J. Bai, J. Ren and X. Qu, *Angew. Chem., Int. Ed.*, 2025, **64**, e202505742.
9 G. Li, H. Liu, T. Hu, F. Pu, J. Ren and X. Qu, *J. Am. Chem. Soc.*, 2023, **145**, 16835–16842.
10 S. Li, L. Shang, B. Xu, S. Wang, K. Gu, Q. Wu, Y. Sun, Q. Zhang, H. Yang, F. Zhang, L. Gu, T. Zhang and H. Liu, *Angew. Chem., Int. Ed.*, 2019, **58**, 12624–12631.
11 D. Han, K. Yang, L. Chen, Z. Zhang, C. Wang, H. Yan and J. Wen, *Chem. Sci.*, 2024, **15**, 6002–6011.
12 Y. Chen and G. Yang, *J. Phys. Chem. Lett.*, 2022, **13**, 11770–11777.
13 C. Wang, H. Wang, B. Xu and H. Liu, *View*, 2021, **2**, 20200045.
14 S. Li, X. Zhu, H. Liu and B. Sun, *Coord. Chem. Rev.*, 2024, **518**, 216046.
15 C. Zhong, C. Hu, D. Ouyang, A. Dan, Y. Zhong, Z. Cai and Z. Lin, *Chem. Eng. J.*, 2023, **477**, 146979.
16 J. Zhao, L. Wang, L. Jia, Y. Liu, S. Cao, J. Wen, W. Li and K. Yang, *Small*, 2025, **21**, 2408959.
17 T. Wu, F. Han, J. Mei, J. Chen, P. Li, M. Li, J. Shen, X. Han, R. Song, S. Hou, X. Li, Y. Su, W. Yue and B. Sun, *J. Colloid Interface Sci.*, 2025, **699**, 138178.
18 M. Talebi, K. Dashtian, R. Zare-Dorabei, H. Ghafuri, M. Mahdavi and F. Amourizi, *Anal. Chim. Acta*, 2023, **1247**, 340924.
19 S. Manzoor, M. A. Younis, Y. Yao, Q.-u.-n. Tariq, B. Zhang, B. Tian, L. Yan and C. Qiu, *Coord. Chem. Rev.*, 2025, **541**, 216840.
20 B. Mishra, A. Alam, A. Chakraborty, B. Kumbhakar, S. Ghosh, P. Pachfule and A. Thomas, *Adv. Mater.*, 2024, 2413118.
21 T. Ogoshi, T.-a. Yamagishi and Y. Nakamoto, *Chem. Rev.*, 2016, **116**, 7937–8002.
22 X. Li, X. Niu, P. Fu, Y. Song, E. Zhang, Y. Dang, J. Yan, G. Feng, S. Lei and W. Hu, *Appl. Catal. B Environ. Energy*, 2024, **350**, 123943.
23 Z.-Q. Wang, M.-H. Li, S. Liang, Y. Kong, C. Wang, L. Li, J.-J. Xu and Y.-W. Yang, *J. Am. Chem. Soc.*, 2025, **147**, 13618–13628.
24 L. Liu, Y. Hu, S. Huang, Y. Jin, J. Cui, W. Gong and W. Zhang, *Chem. Sci.*, 2021, **12**, 13316–13320.
25 L. Hu, Y. Cai, X. Guo, L. Wang, Y. Jiang, X. Li, N. Liu, W. Feng and L. Yuan, *Angew. Chem., Int. Ed.*, 2025, **64**, e202510534.
26 Y. Pan, R. Qin, M. Hou, J. Xue, M. Zhou, L. Xu and Y. Zhang, *Sep. Purif. Technol.*, 2022, **300**, 121831.
27 W. Lin, J. Lin, X. Zhang, L. Zhang, R. A. Borse and Y. Wang, *J. Am. Chem. Soc.*, 2023, **145**, 18141–18147.
28 V. Dippold, S. Vogl, J. Grüneberg and A. Thomas, *Macromol. Rapid Commun.*, 2023, **44**, 2300046.
29 W. Zhang, Z. Lu, C. Chen, P. Vannatta, C. Yang, A. M. Al-Enizi, A. Nafady and S. Ma, *Small*, 2025, **21**, 2502316.
30 E. M. Johnson, R. Haiges and S. C. Marinescu, *ACS Appl. Mater. Interfaces*, 2018, **10**, 37919–37927.
31 W. Wu, Z. Li, S. Liu, D. Zhang, B. Cai, Y. Liang, M. Wu, Y. Liao and X. Zhao, *Angew. Chem., Int. Ed.*, 2024, **63**, e202404563.
32 Z. Xu, Q. Duan and X. Cui, *Chem. Eng. J.*, 2025, **511**, 162241.
33 X. Liu, R. Qi, S. Li, W. Liu, Y. Yu, J. Wang, S. Wu, K. Ding and Y. Yu, *J. Am. Chem. Soc.*, 2022, **144**, 23396–23404.
34 Y. Bai, W. Gao, J. Wei, B. Yu, L. Zhang, P. Zhu and J. Yu, *Chem. Eng. J.*, 2024, **490**, 151628.
35 C. Liu, H. Li, F. Liu, J. Chen, Z. Yu, Z. Yuan, C. Wang, H. Zheng, G. Henkelman, L. Wei and Y. Chen, *J. Am. Chem. Soc.*, 2020, **142**, 21861–21871.
36 J. Wang, X. Yang, T. Wei, J. Bao, Q. Zhu and Z. Dai, *ACS Appl. Bio Mater.*, 2018, **1**, 382–388.
37 Y. Dai, Y. Ding and L. Li, *Chin. Chem. Lett.*, 2021, **32**, 2715–2728.
38 C. Wang, K. Yang, T. Li, L. Jia, H. Yan and J. Wen, *Small*, 2025, **21**, 2500558.